

RESEARCH ARTICLE | MAY 23 2022

Valve-mediated flow control in salp-like locomotion

Xiaobo Bi (毕晓波); Hui Tang (唐辉) ; Qiang Zhu (朱强)  



Physics of Fluids 34, 051913 (2022)

<https://doi.org/10.1063/5.0096004>



CrossMark

Valve-mediated flow control in salp-like locomotion



Cite as: Phys. Fluids **34**, 051913 (2022); doi: [10.1063/5.0096004](https://doi.org/10.1063/5.0096004)

Submitted: 14 April 2022 · Accepted: 29 April 2022 ·

Published Online: 23 May 2022



View Online



Export Citation



CrossMark

Xiaobo Bi (毕晓波),¹ Hui Tang (唐辉),¹ and Qiang Zhu (朱强)^{2,a)}

AFFILIATIONS

¹Department of Mechanical Engineering, The Hong Kong Polytechnic University, Hung Hom, Kowloon, Hong Kong 999077, People's Republic of China

²Department of Structural Engineering, University of California San Diego, La Jolla, California 92093-0085, USA

^{a)} Author to whom correspondence should be addressed: qizhu@ucsd.edu

ABSTRACT

By using an axisymmetric model, we numerically investigate the underlying fluid dynamics of a salp-like swimmer consisting of a deformable shell, a front valve, and a back valve. Through coordinated shell inflation/deflation and valve opening/closing, uni-directional flow is created inside the body and in the wake, which provides thrust for forward motion. Our results prove that this method is capable of sustained locomotion. The uni-directional internal flow successfully reduces energy loss due to dissipation inside the body. Moreover, due to hydrodynamic interactions among different body parts (i.e., the shell and the two valves), the energy expenditure of one part may be recovered by others. In addition to its benefit to energy efficiency, this phenomenon also implies that the valves may be passively activated by harvesting energy spent by the shell, so that the mechanical design can be simplified. Parametric studies have been conducted to determine the effect of the stroke ratio. Furthermore, the locomotion performance of the salp-like system has been compared with that of a squid-like system in which the refilling flow and the jet are in opposite directions.

Published under an exclusive license by AIP Publishing. <https://doi.org/10.1063/5.0096004>

I. INTRODUCTION

Jetting is a straightforward measure of momentum exchange between an object and its environment to produce thrust or maneuvering forces. In nature, jet propulsion is a locomotion mode utilized exclusively by aquatic creatures such as jellyfish, cephalopods (squid, octopus, and cuttlefish), pelagic cnidarians, and tunicates (e.g., salps). This may be attributed to the fact that due to the high density of water, formation of a water jet provides large repulsive force. In addition, with the buoyancy force underwater, it is relatively easy to balance one's self-weight so that the aquatic environment is more tolerant for different locomotion methods.

In comparison with other jet swimmers, the swimming method of salps is unique since it is characterized by uni-directional flow throughout the whole refilling–jetting cycle.^{1,2} Salps live in two different stages during their life cycles, solitary and aggregate. In both stages, pulsed jetting is the primary way of locomotion. As shown in Fig. 1, the body of a salp-like swimmer has two openings in opposite ends. The one in front is called the oral syphon. The one at the back is the atrial syphon. Both can be open or closed. A complete cycle of jet propulsion includes two phases, i.e., refilling and jetting. During the refilling phase, the oral syphon is open and the atrial syphon is closed when

the body expands to allow water in. During the jetting phase, the body shrinks, meanwhile the oral syphon shuts and the atrial syphon opens to let the water out. By reversing the opening and shutting sequence of the oral and atrial syphons, the swimming direction can be easily switched from head-first to tail-first. Both the inflow during inflation and the outflow during deflation are in the opposite direction of the swimming direction so that the flow inside the chamber is mostly uni-directional, unlike the internal flow fields of other jet-propelled swimmers. For example, in the jet swimming mode of squid, water is sucked into its mantle cavity via mantle aperture during the refilling phase and ejected through its funnel tube during the jetting phase.³ Since both the mantle aperture and the funnel tube are near the head, the refilling flow and the jet flow are in opposite directions. As demonstrated in recent simulations, instead of contributing to the jet (and, subsequently, the thrust generation), the kinetic energy of the refilling flow is mostly dissipated inside the pressure chamber due to viscosity.⁴ Therefore, in that scenario, it is desirable to slow down the refilling flow (e.g., by increasing the size of the inlet) to improve energy efficiency. It is not clear what kind of role the refilling flow plays in salp-like locomotion when it is in the same direction of the jet.

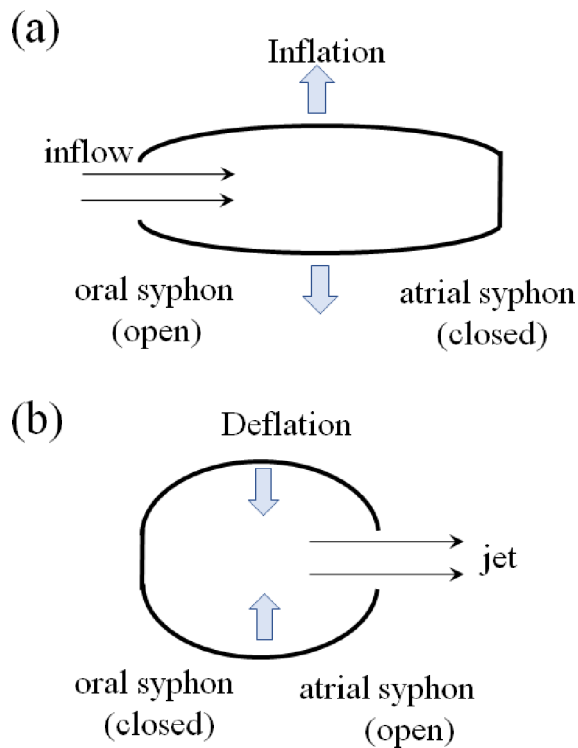


FIG. 1. Schematic illustration showing the body configuration and flow direction of salp-like jet propulsion during (a) refilling and (b) jetting phases.

Among all the aquatic swimming methods, the undulation/flapping mode of fish and marine mammals has attracted most of the attention. There is also a growing interest in the propulsion mechanism of jellyfish and cephalopods. Specifically, it was suggested that squid might be a good prototype for high-speed soft-bodied underwater robots.^{5–8} However, there has been very little work about the fluid dynamics of salps. One of the existing studies about salp swimming is the experimental investigation of the flow fields near live salps via particle image velocimetry (PIV).⁹ This study illustrates two distinctive vorticity patterns in the wake, mode I and mode II. In mode I, the discharged vorticity after each jetting is mostly entrained into a leading vortex ring. Mode II, on the other hand, features a leading vortex ring followed by a long trailing wake with weaker vortices. These flow patterns were also observed in wakes of swimming squid¹⁰ or a simple piston–cylinder device.¹¹ By measuring the speed of the jet, the thrust generation and propulsive efficiency were also estimated. However, the efficiency was calculated by using a simplified model based on quasi-steady assumption,¹² whose accuracy in the highly unsteady pulsed-jet scenario is questionable.¹³ Based on theoretical analysis, Sutherland and Weihs pointed out that in the aggregate form, salps achieved better locomotion performance since the asynchronous jetting of individuals led to less oscillations in the forward speed.¹⁴ This type of multijet propulsion has been numerically studied using a computational fluid dynamics solver based on the software package ANSYS FLUENT.¹⁵ The focus was on the effect of the jet angle upon the performance of the system. A quasi-steady problem was studied without considering the unsteady

fluid–structure interaction procedure during the refilling and jetting cycles.

The purpose of the current study is not to duplicate the exact geometry, morphology, and kinematics of salps in jet-propelled locomotion. Instead, we concentrate on a simple salp-inspired system that utilizes the same locomotion mechanism to illustrate the underlying physics of this biological system and shed light on the possibility of bio-inspired applications. The system we study consists of an empty chamber (the pressure chamber) enclosed within a deformable shell, an inlet, and an outlet. The open and closed states of the inlet/outlet are controlled by valves. The deformation of the shell and the motions of the valves are prescribed, whereas the forward motion of the body is determined via Newton’s law.

The rest of the paper is organized as follows. We start by defining the geometry and kinematics of the physical system, i.e., the idealized slap-like swimmer. This is followed by a brief description of the governing equations and numerical method. Details about the numerical model as well as validations are included in our previous publications. In Sec. IV, the locomotion performance of the system and the characteristics of the flow fields around and inside the body will be presented and discussed. Finally, conclusions are drawn.

II. PROBLEM DEFINITION

As shown in Fig. 2, we consider the self-propelled locomotion of an axisymmetric object consisting of a deformable shell and two valves (the front and back ones) that can be opened and shut. With x as the axis of symmetry and r the axis in radial direction, the contour of the shell forms a semi-elliptical shape whose major axis is L and the semi-minor axis is a . The diameters of the inlet and the outlet are D . Within the x – r plane, both the front valve and the back valve remain straight with rotational angles θ_1 and θ_2 , respectively. When these angles are zero, the corresponding valve is closed. When they are $\pi/2$, the valve is fully open. Otherwise, the valve is partially open.

Within a deformation period $t \in [0, T]$, the length L is fixed while the semi-minor axis a varies so that

$$a = a(t) = a_0 + (a_1 - a_0)[1 - \cos(2\pi t/T)]/2, \quad (1)$$

where a_0 and a_1 are the values of a in deflated and inflated states, respectively.

Meanwhile, the rotational angles of the two valves are

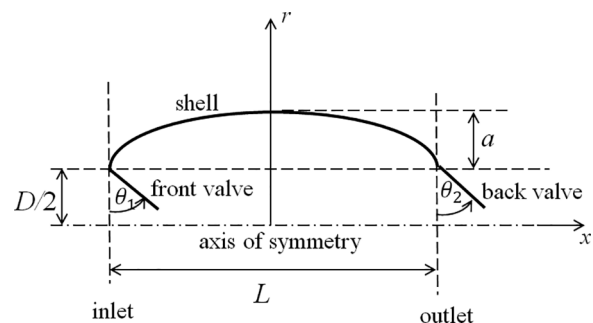


FIG. 2. An idealized model of a salp-like swimmer.

$$\theta_1(t) = \begin{cases} \pi t/(2t_0), & 0 \leq t < t_0, \\ \pi/2, & t_0 \leq t < T/2, \\ \pi(T/2 + t_0 - t)/(2t_0), & T/2 \leq t < T/2 + t_0, \\ 0, & T/2 + t_0 \leq t \leq T, \end{cases} \quad (2)$$

and

$$\theta_2(t) = \begin{cases} \pi(t_0 - t)/(2t_0), & 0 \leq t < t_0, \\ 0, & t_0 \leq t < T/2, \\ \pi(t - T/2)/(2t_0), & T/2 \leq t < T/2 + t_0, \\ \pi/2, & T/2 + t_0 \leq t \leq T. \end{cases} \quad (3)$$

Here, t_0 is the time it takes for the opening and closing processes of the valves. According to Eqs. (1)–(3), the first half period ($0 \leq t < T/2$) is the inflation phase, during which the opening of the front valve and the closing of the back valve take place when $0 \leq t < t_0$. In the rest of the inflation phase ($t_0 \leq t < T/2$), the front valve remains open and the back one is closed. The second half period ($T/2 \leq t \leq T$) corresponds to the deflation phase, at the beginning of which ($T/2 \leq t < T/2 + t_0$) the front valve is closed and the back valve opens, and they remain in these states until the end of the cycle. The coordinated deformation of the body and the motion of the valves are illustrated in Fig. 3.

There are two dimensionless parameters that play important roles in this problem. One is the stroke ratio Γ_m , defined as $4\Delta V/(\pi D^3)$, where ΔV is the discharged volume during a single jetting. The other one is the jet-related Reynolds number Re , defined as $\rho D \bar{u}/\mu$, where \bar{u} is the peak value of the spatially averaged inflow (or outflow) speed at the inlet (or outlet). ρ is the density of the fluid and μ is its dynamic viscosity.

III. MATHEMATICAL FORMULATION AND NUMERICAL MODEL

A. Fluid dynamics equations

Since the flow is incompressible and the problem is axisymmetric, we invoke the axisymmetric version of the incompressible Navier–Stokes equations and the continuity equation for mathematical description of the underlying physics, so that

$$\rho \left(\frac{\partial u_x}{\partial t} + u_x \frac{\partial u_x}{\partial x} + u_r \frac{\partial u_x}{\partial r} \right) = -\frac{\partial p}{\partial x} + \mu \left(\frac{\partial^2 u_x}{\partial x^2} + \frac{\partial^2 u_x}{\partial r^2} + \frac{\partial u_x}{r \partial r} \right) + f_x, \quad (4)$$

$$\rho \left(\frac{\partial u_r}{\partial t} + u_x \frac{\partial u_r}{\partial x} + u_r \frac{\partial u_r}{\partial r} \right) = -\frac{\partial p}{\partial r} + \mu \left(\frac{\partial^2 u_r}{\partial x^2} + \frac{1}{r} \frac{\partial}{\partial r} \left(r \frac{\partial u_r}{\partial r} \right) - \frac{u_r}{r^2} \right) + f_r, \quad (5)$$

$$\frac{\partial u_x}{\partial x} + \frac{1}{r} \frac{\partial (ru_r)}{\partial r} = 0, \quad (6)$$

where $\mathbf{x} \equiv (x, r)$ is the position vector in the cylindrical coordinate system x - r . $\mathbf{u} \equiv (u_x, u_r)$ is the flow velocity, and p is the pressure. f_x and f_r are the x - and r -components of the force \mathbf{f} exerted on the fluid by the structure. In the immersed-boundary formulation, this force is related to the fluid-applied force $\mathbf{F} \equiv (F_x, F_r)$ on the structure via the two-dimensional Dirac delta function δ . We have

$$\mathbf{f}(\mathbf{x}, t) = \int_{\Gamma_i} \mathbf{F}(s, t) \delta(\mathbf{X}(s, t) - \mathbf{x}) ds \quad (7)$$

and

$$\mathbf{F}(s, t) = \alpha \int_0^t [\mathbf{U}(s, \tau) - \mathbf{V}(s, \tau)] d\tau + \beta [\mathbf{U}(s, t) - \mathbf{V}(s, t)], \quad (8)$$

where Γ_i stands for the structural surface (the shell and the valves) with s being a Lagrangian coordinate along it. In the current study, variations of the body position \mathbf{X} and the body velocity $\mathbf{V}(s, t) \equiv \partial \mathbf{X}(s, t)/\partial t$ contain two parts, the prescribed deformation, including the expansion and shrinking of the shell and the opening/closing of the two valves described in Sec. II, and the forward motion which is going to be determined via Newton’s law (see Sec. III B). The parameters α and β are applied to enforce the consistency in terms of velocities and positions between neighboring fluid and structure elements so that the no-flux and no-slip conditions at the fluid–structure interface are satisfied. When their values are sufficiently large, they have no effect on the results. \mathbf{U} is the fluid velocity at the fluid–solid interface calculated as

$$\mathbf{U}(s, t) = \int_{\Omega_f} \mathbf{u}(\mathbf{x}, t) \delta(\mathbf{x} - \mathbf{X}(s, t)) d\mathbf{x}, \quad (9)$$

where Ω_f stands for the fluidic domain.

B. Forward motion

Let m_b be the mass of the body and x_b be the displacement of the center of mass of the solid structure in the $-x$ direction (hereby we neglect the mass of the two valves and assume that the mass of the shell is evenly distributed), according to Newton’s law we have

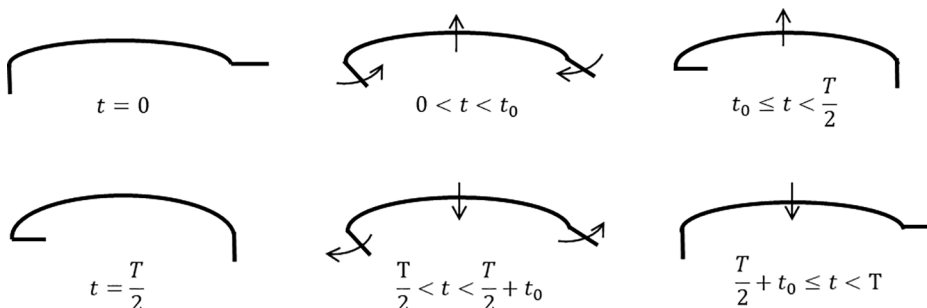


FIG. 3. Coordinated body deformation and valve motion during a cycle.

$$m_b \ddot{x}_b = F_{net}, \tag{10}$$

where $F_{net} = -\int_{\Gamma_i} 2\pi r(s) F_x(s, t) ds$ is the net force exerted on the body in the $-x$ direction. $F_x(s, t)$ is the distributed interaction force in the x direction along the body.

C. Characterization of performance

An important measure of the swimming performance is the time-averaged swimming speed \bar{u}_b , defined as the time derivative of x_b (i.e., \dot{x}_b) averaged over one swimming cycle (hereafter, we use the symbol “overline” to represent time-averaged values over one cycle T after steady state is established). We use the cost of transport (CoT) to quantify the energy efficiency of the locomotion. CoT refers to the energy expenditure E divided by the traveled distance l . E is obtained by integrating the power expenditure P over time, where

$$P = P_s + P_f + P_b \\ = \int_{\Gamma_{is}} 2\pi r \mathbf{F} \cdot \mathbf{U} ds + \int_{\Gamma_{if}} 2\pi r \mathbf{F} \cdot \mathbf{U} ds + \int_{\Gamma_{ib}} 2\pi r \mathbf{F} \cdot \mathbf{U} ds. \tag{11}$$

Γ_{is} , Γ_{if} , and Γ_{ib} are the shell, the front valve, and the back valve, respectively. In our study, CoT is calculated within a cycle in the steady-swimming state.

To understand the physics of thrust generation, we will employ a thrust-drag decomposition method developed recently.^{13,16} To elaborate, the net force on the body F_{net} is decomposed into two parts, the jet-related thrust F_T and other forces F_D so that $F_{net} = F_T + F_D$. According to control volume analysis¹³ (hereby the control volume includes the space bounded by the shell, the inlet, and the outlet), F_T contains three parts: the momentum flux in and out of the body F_j , the normal fluidic force at the inlet and outlet F_σ , and the internal fluid inertia force F_m . Among these, F_j includes contributions from the momentum flux into the inlet F_{jf} and the momentum flux out of the outlet F_{jb} so that $F_j = F_{jf} + F_{jb}$. During a cycle $t \in [0, T]$, we have

$$F_{jf} = \begin{cases} -\rho \int_{A_f} u_x(u_x + u_b) d\mathbf{x}, & 0 \leq t \leq T/2 + t_0, \\ 0 & \text{otherwise,} \end{cases} \tag{12}$$

and

$$F_{jb} = \begin{cases} 0, & t_0 \leq t < T/2, \\ \rho \int_{A_b} u_x(u_x + u_b) d\mathbf{x} & \text{otherwise.} \end{cases} \tag{13}$$

Here, A_f and A_b stand for the areas of inlet and outlet, respectively. u_b , again, is the forward speed of the center of mass of the shell, which coincides with the speeds of the inlet and the outlet since the length of the body remains unchanged. Note that the inflow at the inlet brings negative momentum with respect to the swimming direction into the internal flow field so that it contributes negatively to thrust generation. The outflow at the outlet, on the other hand, takes negative momentum out of the internal chamber so that its contribution to thrust is positive.

The normal forces at the inlet and the outlet are calculated as

$$F_{\sigma f} = \begin{cases} -\rho \int_{A_f} (-\sigma - p_\infty) d\mathbf{x}, & 0 \leq t \leq T/2 + t_0, \\ 0 & \text{otherwise,} \end{cases} \tag{14}$$

and

$$F_{\sigma b} = \begin{cases} 0, & t_0 \leq t < T/2, \\ \rho \int_{A_b} (-\sigma - p_\infty) d\mathbf{x} & \text{otherwise,} \end{cases} \tag{15}$$

where σ is the normal stress at the inlet or the outlet, which contains the pressure and the normal viscous stress. p_∞ is the far-field pressure.

The inertia force of the internal flow is

$$F_m = \rho \frac{\partial}{\partial t} \int_{\Omega} u_x d\mathbf{x}, \tag{16}$$

where Ω is the internal volume surrounded by the deformable shell, the inlet, and the outlet.

The thrust-drag decomposition method was originally developed for the definition of a propulsive efficiency of a system driven solely by jet propulsion. The current salp-like system includes not only jet flow but also rotational motions of the valves. For example, the opening and closing motions of the back valve occur outside of the control volume (which includes the internal flow field only) so that its effect on thrust generation is not counted for. For this reason, in terms of the energetic performance of the system, the CoT is a more reliable measure of energetic efficiency. Nevertheless, the force decomposition method provides unique insights into the underlying physics of the detailed mechanism of thrust generation.

D. Numerical method

We employ a finite-difference algorithm to solve Eqs. (4)–(6). In this approach, the spatial discretization is achieved by using a second-order algorithm in staggered grids. The time integration is conducted using a Crank–Nicholson algorithm. The implicit treatment of the convective term makes the equations nonlinear; therefore, we linearize the system with a second-order temporal factorization method.¹⁷ These treatments lead to a discrete linear system of equations which can be solved using a projection method. In this method, the velocity and pressure are decoupled by using the block lower triangular–upper triangular decomposition method. A provisional velocity field is obtained based on the flow field information at the previous time step. It is then used to update the pressure field (hereby we employ the BiCGSTAB iterative method along with the incomplete LU (ILU) preconditioner to solve the elliptic pressure equation). Afterwards, the flow velocity field is updated with the new pressure field to fulfill mass conservation. More details about the numerical strategy applied in this study are included in an earlier paper¹⁸ and our previous publications.^{13,19} The accuracy and fidelity of the numerical method have been extensively tested in these publications through comparisons with benchmark results of canonical problems.

IV. RESULTS

The problem is normalized by choosing the body length L , the fluid density ρ , and the deformation cycle T as the repeating variables. Therefore, hereafter we have $L = 1$, $\rho = 1$, and $T = 1$. Unless otherwise specified, in the following simulations some parameters are fixed, including the time for valve closing and opening processes ($t_0 = 0.1$), the dynamic viscosity of the fluid ($\mu = 0.001$), the mass of the body ($m_b = 0.05$), and the length of the semi-minor axis of the shell in its deflated state ($a_0 = 0.05$).

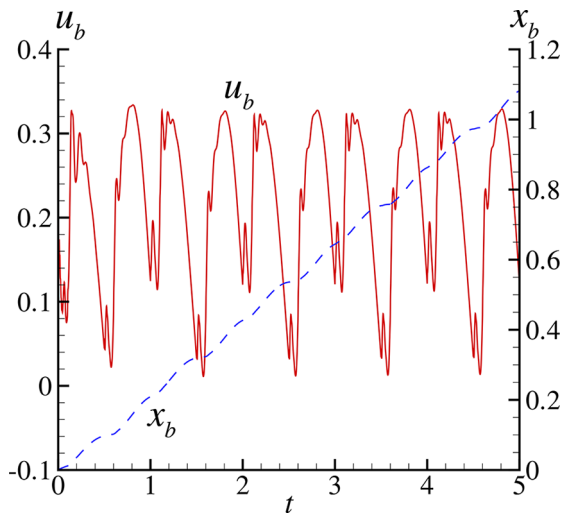


FIG. 4. Time histories of the forward speed u_b and forward displacement x_b . $a_1 = 0.07$. $D = 0.15$.

Following numerical tests in previous studies,^{13,19} the simulations of this study are performed in a 15×1 rectangular domain. The finest fluidic grid near the body is set to be $\Delta x = \Delta r = 0.003$. 600 uniformly distributed grids are used along the body

(including the shell and the two valves). The time step is fixed at $\Delta t = 10^{-4}$.

To accommodate the finite size of the computational domain and prevent the body from moving out of it, a uniform incoming flow is introduced to offset the forward motion of the system. For this purpose, the speed of this flow is chosen numerically to roughly match the results (e.g., the speed of the system and the body displacement) is removed during post processing.

A. Dynamic features of self-propelled locomotion

We start by considering a representative case in which $a_1 = 0.07$ and $D = 0.15$. The corresponding Reynolds number and stroke ratio of this case are $Re = 332$ and $\Gamma_m = 4.69$, respectively.

Figure 4 shows the time histories of the forward speed u_b and the displacement x_b . The curve for u_b clearly includes disturbances caused by the rotational motions of the front and back valves at the beginning of the inflation and deflation phases. The steady state is established after 1–2 cycles. Afterwards, the time-averaged forward speed \bar{u}_b is 0.22.

From now on all the time histories of physical quantities and snapshots of flow fields will be obtained within a deformation cycle after the steady state is reached. For convenience, the starting time of the cycle to display is shifted to zero.

In Fig. 5, we plot time histories of the thrust components due to momentum flux and normal stress at the inlet and outlet, as well as

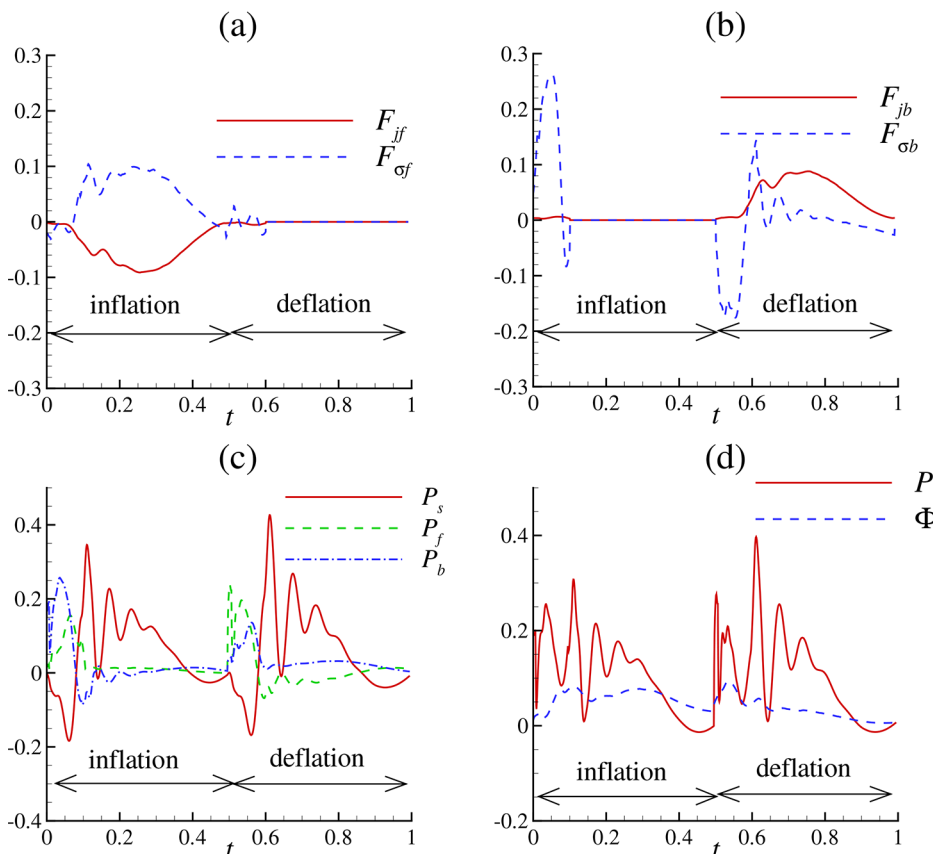


FIG. 5. Time histories over one cycle of (a) the momentum-flux-related and the normal-stress-related thrusts at the inlet, (b) the momentum-flux-related and the normal-stress-related thrusts at the inlet, (c) the power expenditures of the shell, the front valve, and the back valve, and (d) the total power expenditure and the rate of energy dissipation in the chamber. $a_1 = 0.07$. $D = 0.15$.

the power expenditures and the rate of energy dissipation of the internal flow field Φ , which is calculated as

$$\Phi = \int_{\Omega} \phi d\mathbf{x}, \tag{17}$$

where ϕ is given as

$$\phi = 2\mu \left[\left(\frac{\partial u_r}{\partial r} \right)^2 + \left(\frac{u_r}{r} \right)^2 + \left(\frac{\partial u_x}{\partial x} \right)^2 \right] + \mu \left(\frac{\partial u_x}{\partial r} + \frac{\partial u_r}{\partial x} \right)^2. \tag{18}$$

According to Fig. 5(a), during the inflation phase F_{jf} is negative while F_{of} is positive. This is due to the fact that when fluid flows into the internal chamber from the inlet, it brings negative momentum with respect to the swimming direction. Meanwhile, there is a negative pressure at the inlet (unless the Reynolds number is very small, F_{of} is dominated by pressure), which creates suction force that pulls the body forward. During most of the deflation phase both F_{jf} and F_{of} are zero since the front valve is closed. Overall, the time-averaged values of F_{jf} and F_{of} are $\bar{F}_{jf} = -2.39 \times 10^{-2}$ and $\bar{F}_{of} = 2.35 \times 10^{-2}$. Thus, the mean contribution of the inlet to thrust is almost zero.

At the outlet [Fig. 5(b)], the momentum flux thrust component F_{jb} behaves similarly to F_{jf} , despite the fact that it mostly exists during the deflation phase and its value is positive. The normal stress component F_{ob} , on the other hand, is very different from its counterpart F_{of} at the inlet. The most pronounced feature is its large absolute values at the beginning of inflation and deflation phases. This phenomenon is explained by the motion of the valves and their effect on the pressure distribution in the flow field. As shown in Fig. 6(a), at the beginning of the inflation phase both the front valve and the back valve rotate inwards, leading to high pressure inside the chamber. The outlet resides within this high pressure zone [i.e., the zone in red in Fig. 6(a)] so that large positive F_{ob} is produced. On the other hand, the inlet lies out of this zone and the pressure there is close to outside pressure so that F_{of} is relatively small at this moment. At the beginning of the deflation phase, the front and back valves rotate outwards, creating low pressure in the chamber and negative F_{ob} [Fig. 6(b)]. Again, the inlet lies beyond this zone and F_{of} is not affected.

The averaged values of F_{jb} and F_{ob} are $\bar{F}_{jb} = 2.32 \times 10^{-2}$ and $\bar{F}_{ob} = 6.25 \times 10^{-3}$. Both are positive, indicating that the outlet contributes positively to thrust generation.

The thrust component due to the inertia of fluid inside the chamber, F_m , is also obtained from the simulation. The time-averaged value

of this component is $\bar{F}_m = 1.66 \times 10^{-4}$, which is much smaller than other thrust components. This is consistent with our conclusion for squid-like jetting.⁴ For this reason, we are not going to discuss this thrust component in detail.

The time histories of the power expenditures of the shell and the valves (P_s , P_f and P_b) are shown in Fig. 5(c). A notable feature is that at the beginning of the inflation and deflation phases the power expenditure of the shell P_s is negative. This phenomenon can also be explained by the pressure distribution at these instants shown in Fig. 6. As the beginning of the inflation phase the rotations of the two valves cause high pressure inside the chamber, which pushes the shell out so that its expansion at this moment is passive. Similarly, at the beginning of the deflation phase there is low pressure inside the chamber so that the shell is sucked in without any activation force applied. The implication is that the particular kinematics chosen in our study may be an effective way of energy saving through coordinated motion and deformation of the body and the valves.

After the valves stop rotating, there are still oscillations in P_s , which are attributed to the evolution of vortices inside the chamber as illustrated in Sec. IV C.

The average power expenditure \bar{P} ($P = P_s + P_f + P_b$) in this case is found to be 0.104. Correspondingly, the cost of transport CoT is 0.474.

It is necessary to point out that the scenario discussed above, i.e., the energy expended by the valves is partially recaptured by the shell, is not the only mode of hydrodynamic interaction between the shell and the valves. For example, in Fig. 7, we display results from a case in which the opening/closing time of the valves t_0 is increased from 0.1 to 0.2 while the other parameters remain unchanged. It is seen from Fig. 7(a) that in this case during the opening and closing motions of the valves P_s remains positive, whereas P_f and P_b are negative so that the valves are able to harvest energy spent by the shell. This is explained by the pressure distributions shown in Fig. 7(b). As inflation starts, the rotations of the two valves in this case are relatively slow so that the pressure inside the chamber is low since it is determined mostly by the expansion of the shell. When this happens the opening and closing motions of the valves can actually be passively activated by the pressure gradient and no external energy input is needed. Similarly, when deflation starts the shrinking shell creates high pressure inside the chamber, which pushes the valves to their desired positions without external intervention.

These examples show that during the hydrodynamic interactions among different parts of the system the direction of energy flow depends on the system kinematics—the parts that make stronger disturbance donate energy to the flow field while others recover it. With the particular rotational directions depicted in Eqs. (2) and (3), the valves can be passively activated if the deformation of the shell causes sufficient disturbance to the internal flow field. As shown in Fig. 8, among all the possible designs of the rotational directions of the valves, only in design 0 (i.e., the one used in the current study) the front and back valves rotate in the same direction as the local flow in both inflation and deflation so that it requires less (or no) external energy input to activate them. It is going to significantly simplify the mechanical and control system. This is a key advantage of this design over others.

Another indicative quantity of the system energetics is the rate of energy dissipation Φ inside the chamber. According to our previous study,⁴ in squid-like jetting the kinetic energy of the flow into the

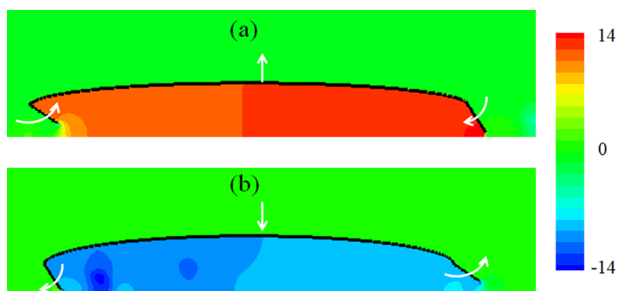


FIG. 6. Snapshots of pressure distribution at (a) $t = T/16$ and (b) $t = 9T/16$. The arrows show the moving directions of the shell, the front valve, and the back valve. $a_1 = 0.07$. $D = 0.15$.

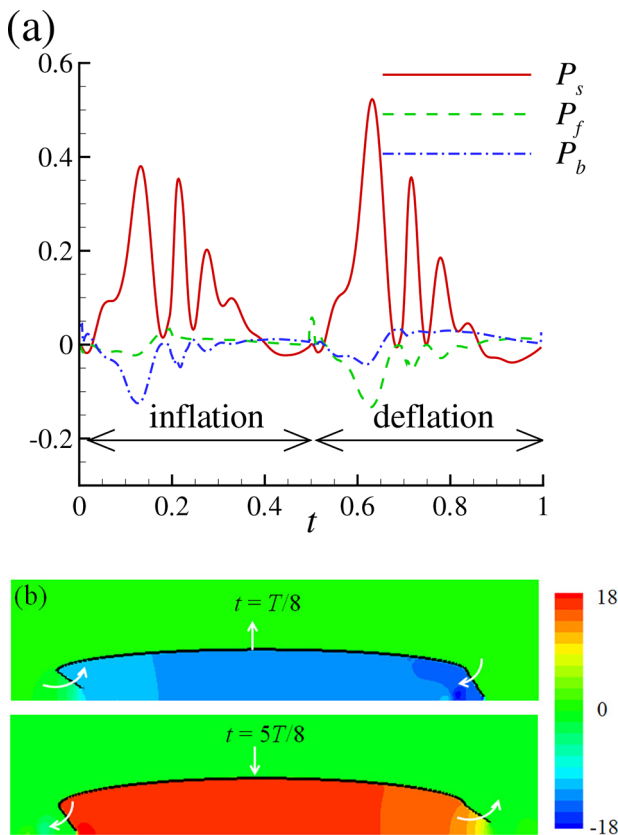


FIG. 7. (a) Time histories over one cycle of the power expenditures of the shell, the front valve, and the back valve. (b) Snapshots of the pressure distribution at $t = T/8$ and $t = 5T/8$. The arrows show the moving directions of the shell, the front valve, and the back valve. The physical parameters are the same as those in the case shown in Figs. 4 and 5 except that the opening/closing time of the valves $t_0 = 0.2$.

pressure chamber during refilling is mostly dissipated before jetting happens. This is due to the fact that the inflow is in the opposite direction of the jet so that the direction of flow inside the chamber has to be reversed as the swimmer switches from the refilling phase to the jetting phase. In a salp-like swimmer, the scenario is completely different. As shown in Fig. 5(d), the rate of dissipation Φ remains small in comparison with the power input P in both the refilling and the jetting phases.

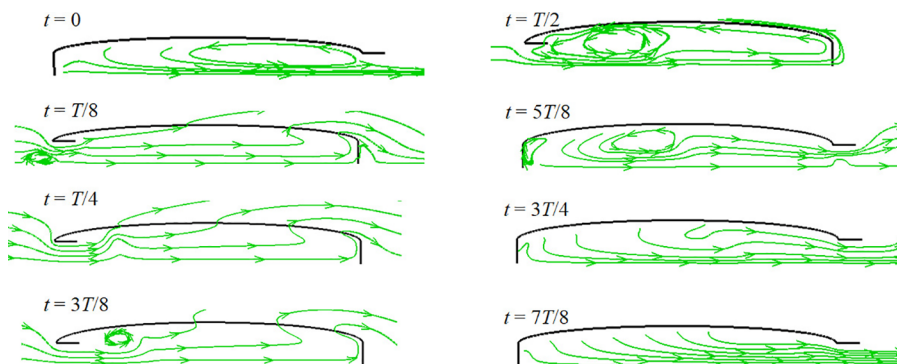


FIG. 9. Streamlines in a body-fixed reference system within a cycle. $a_1 = 0.07$. $D = 0.15$.

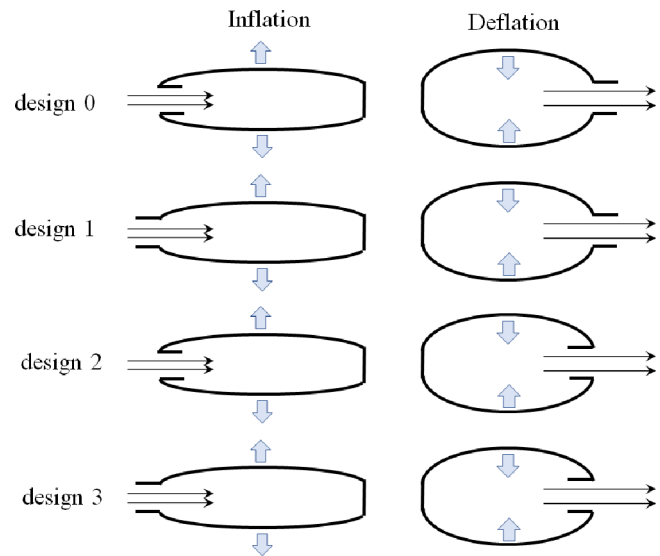


FIG. 8. Possible designs of the rotational directions of the front and back valves.

For insight, in Fig. 9 we plot snapshots of the streamlines inside the salp-like body over one cycle T . It is clear that in this locomotion mode no large-scale flow direction reversal occurs inside the body, and there is no need to eliminate the kinetic energy of the refilling flow.

B. Effect of stroke ratio

A key parameter that determines the wake feature and potentially the locomotion performance of a pulsed-jet swimmer such as the one we are studying is the stroke ratio Γ_m , which physically corresponds to the length to diameter ratio of the jet plug created after each complete deflation. The effect of this parameter was initially examined via piston-cylinder experiments.¹¹ It was demonstrated that there existed a critical value of Γ_m , called the formation number, which marks the transition between two different wake features. When Γ_m is below the formation number, the wake contains a single leading vortex ring fed by a vorticity trail behind it. Above it, the trailing vorticity zone breaks into individual vortices and disconnect from the leading vortex in a phenomenon called pinchoff. After pinchoff the strength of the leading

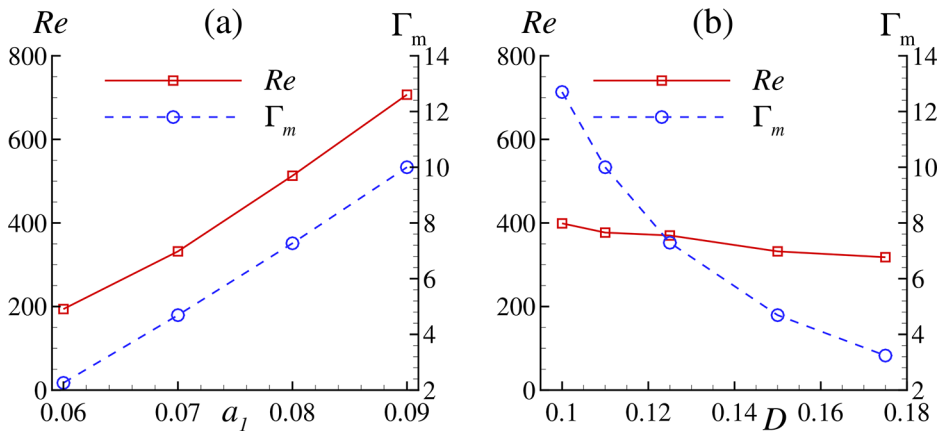


FIG. 10. Variations of the Reynolds number Re and the stroke ratio Γ_m when (a) D is fixed at 0.15 while a_1 varies between 0.06 and 0.09, and (b) a_1 is fixed at 0.07 while D varies between 0.10 and 0.175.

vortex ring stops growing. The exact value of the formation number depends on factors such as the time history of the jet speed (i.e., the jet speed program). When the speed is constant it is around 4.

Moreover, it was found that the formation number correlates with the formation of the “optimal” vortex ring which contains maximum impulse, circulation, and volume for a given energy input.^{20,21} The implication is that the formation number may be associated with optimal locomotion performance via pulsed jetting. A recent experiment with a squid-inspired artificial swimmer demonstrated that by fixing the power input while changing the stroke ratio via the size of the nozzle, the maximum swimming speed was reached when the stroke ratio was around 4.⁷ However, the evidence is not yet conclusive since other factors (e.g., the jet speed program) may also play a role in this system.

Indeed, the effect of stroke ratio is complicated since it also depends on parameters such as the Reynolds number. Specifically, at lower Reynolds numbers the phenomena may be different from the aforementioned ones, which occur at higher Reynolds numbers. For example, numerical simulations show that with a constant jet speed program, at a jet-related Reynolds number of $Re = 150$ the trailing wake does not form isolated vortices so that it remains connected to the leading vortex ring (i.e., there is no obvious pinchoff), although the strength of the leading vortex ring does saturate when Γ_m

reaches 6–7.¹⁹ In a numerical free-swimming test at $Re = 100$, it was found that Γ_m did not have a pronounced effect on the swimming speed and the CoT if the peak jet speed is kept unchanged.¹⁶

A parametric study has been conducted to illustrate the effect of the stroke ratio Γ_m upon the dynamics of the salp-like system. The variation of Γ_m is achieved in two ways: varying a_1 while keeping D fixed, and varying D while keeping a_1 fixed. In Fig. 10, it is seen that when D is fixed at 0.15 and a_1 increases from 0.06 to 0.09, the corresponding jet-related Reynolds number Re rises from 194 to 707 since larger a_1 leads to higher jet speed. There is also a significant increase in Γ_m (from 2.26 to 10) due to the increase in discharged volume during each jetting. On the other hand, when D is raised from 0.1 to 0.175 while a_1 stays at 0.07, the Reynolds number remains in the range between 300 and 400 since the effect of increasing jet speed is offset by that of the decreasing length scale D . Meanwhile, the stroke ratio decreases from 12.7 to 3.24.

Figure 11 displays dependencies of \bar{u}_b , \bar{P} and CoT upon Γ_m with fixed D and varying a_1 . Both \bar{u}_b and \bar{P} increase monotonously with Γ_m , while CoT reaches its minimum value when Γ_m is around 4, which coincides with the optimal condition for vortex ring generation by a jet. In the second scenario, i.e., when a_1 is fixed and D varies (Fig. 12), the Γ_m –CoT curve is somewhat similar to the one in Fig. 11 in that there exists a minimum value. Although in this case, the

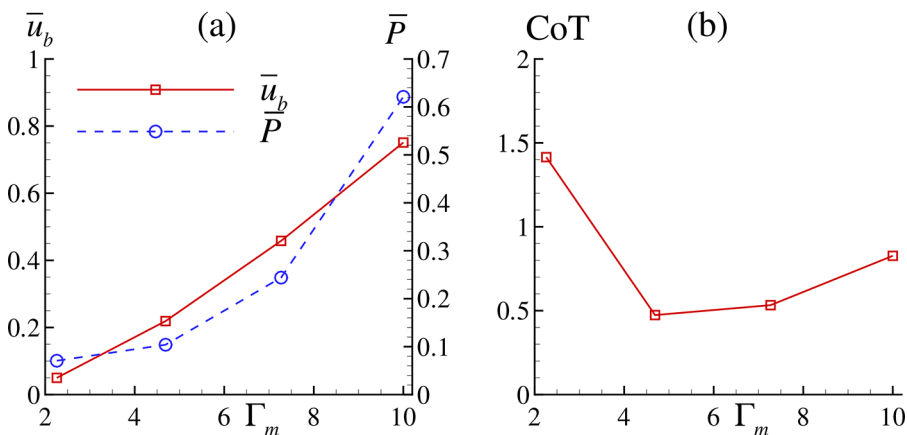


FIG. 11. Dependencies of (a) mean forward speed \bar{u}_b and mean power expenditure \bar{P} and (b) cost of transport CoT upon the stroke ratio Γ_m when D is fixed at 0.15 and a_1 varies between 0.06 and 0.09.

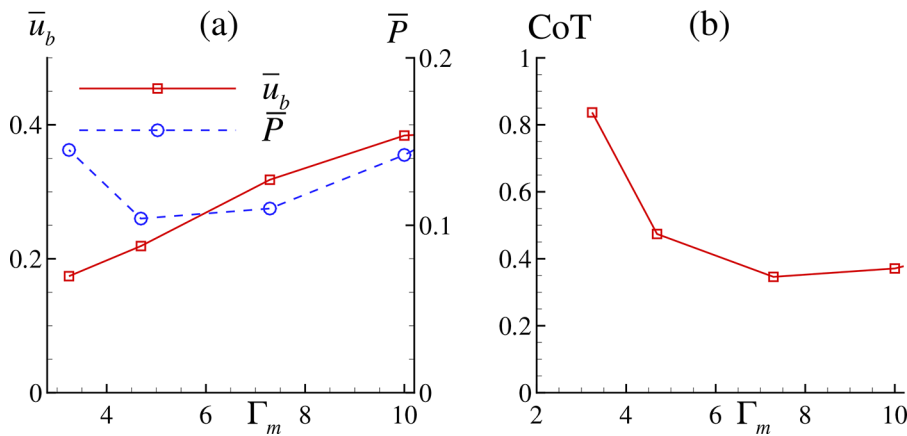


FIG. 12. Dependencies of (a) mean forward speed \bar{u}_b and mean power expenditure \bar{P} and (b) cost of transport CoT upon the stroke ratio Γ_m when a_1 is fixed at 0.07 and D varies between 0.10 and 0.175.

minimum value of CoT is reached when Γ_m is around 7. Meanwhile, \bar{u}_b grows monotonously and \bar{P} plunges to bottom around $\Gamma_m \sim 4$ before it rises again.

One has to be cautious in interpreting the results shown in Figs. 11 and 12, especially the behavior of CoT, which suggest optimal performance not far from the formation number. In comparison with the aforementioned study about dynamics of a squid-inspired swimmer,¹⁶ the current simulations are conducted in higher values of Reynolds number. This might be one of the reasons why the effect of Γ_m on CoT is much more pronounced in our case. However, we note that in comparison with the simple piston-cylinder experiments and theoretical analyses based on them, our problem is much more complicated due to the following factors: (1) Unlike a single jetting process considered in those studies, our system involves repeated jetting and refilling phases so that the forward motion and energy consumption include contributions from both. (2) In the case with fixed D , there is a significant change in Reynolds number when a_1 varies. This is expected to affect the performance of the system. (3) The salp swimming problem is not a pure jet-propulsion problem. The opening and closing motions of the valves consume additional energy and produce thrust or drag forces. This part is particularly important in small stroke ratios when the jet is relatively weak. A possible measure to isolate the thrust generated by jetting is the force decomposition method we developed earlier,¹³ in which the jet-related thrust is obtained as a combination of three parts, the momentum flux at the nozzle, the normal fluidic force at the nozzle, and the inertia force of fluid inside the chamber. However, this method relies on accurate information of flow field at the nozzle (in our case the inlet and the outlet), whereas in the salp-like system the flow fields at the inlet and outlet are heavily disturbed by rotations of the valves (see, e.g., Fig. 6) so that this decomposition method is not able to eliminate influence of the valves on the thrust. Toward this end, development of a better force decomposition method may be necessary.

Incidentally, the locomotion performance of the system is also significantly affected by other parameters, most notably the opening/closing time t_0 of the valves. For example, let us consider the case with $a_0 = 0.05$, $a_1 = 0.07$, and $D = 0.15$ so that the stroke ratio is fixed at 4.69. When $t_0 = 0.1$ the forward speed $\bar{u}_b = 0.22$ and $\text{CoT} = 0.474$. If t_0 is increased to 0.2, \bar{u}_b is reduced to 0.205. Meanwhile, CoT is also reduced to 0.406. The decrease in CoT is explained by the fact that in

this case no extra energy is needed to activate the valves (see Fig. 7). However, if we further increase t_0 to 0.3, \bar{u}_b becomes 0.185 and CoT is increased to 1.31. This suggests that when the valves move too slowly they hinder the inflation and deflation of the body so that more energy is needed to activate the shell deformation.

C. Features of the flow field

In Figs. 13–15, we plot three representative flow fields at low, medium, and high stroke ratios. These flow fields are visualized through contours of vorticity. Negative values of vorticity correspond to counterclockwise vortices and positive values correspond to clockwise vortices.

Figure 13 displays snapshots of the vorticity field over one deformation cycle for a case with $D = 0.15$ and $a_1 = 0.06$ so that its stroke ratio Γ_m is 2.26. When inflation starts ($t = 0$), inside the chamber there is a counterclockwise vortex v_0 , which was generated during the previous cycle. Afterwards, the counterclockwise rotation of the front valve generates a clockwise vortex v_1 (see the snapshot at $t = T/8$). Meanwhile, the clockwise rotation of the back valve generates a counterclockwise vortex, which merges with the wake vorticity nearby so that it is not clearly shown. During inflation, inside the chamber the dominant vortices are the clockwise vortex v_1 created by the rotation of the front valve, a counterclockwise vortex v_2 created by the inflow as it goes through the inlet, and the aforementioned counterclockwise vortex v_0 created in the previous cycle. At the end of the inflation phase ($t = T/2$), the clockwise vortex v_2 is significantly weakened and the vortex v_0 from the previous cycle is almost completely dissipated.

As deflation begins the front valve rotates clockwise and the back valve rotates counterclockwise. The rotation of the front valve generates a counterclockwise vortex, which merges with the existing vortex v_2 in the chamber. The rotation of the back valve generates a clockwise vortex v_3 , which breaks into two parts ($t = 3T/4$). One part is attracted by the counterclockwise vortex from the inlet so that it moves in the $-x$ direction to pair off. The other part joins the counterclockwise vortex created by the jet flow and shed into the wake. At this low value of Γ_m , the vorticity fields associated with the flow into the inlet and the flow out of the outlet are both dominated by single leading vortex rings.

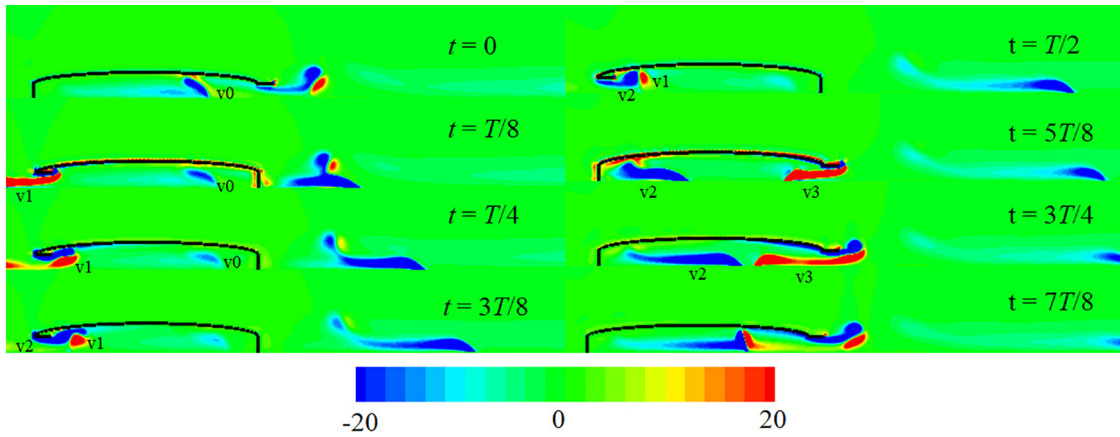


FIG. 13. Snapshots of vorticity distribution around the body within a deformation cycle. $D = 0.15$, $a_1 = 0.06$, $\Gamma_m = 2.26$. Concentrated areas of negative vorticity correspond to counterclockwise vortices; those of positive vorticity correspond to clockwise vortices.

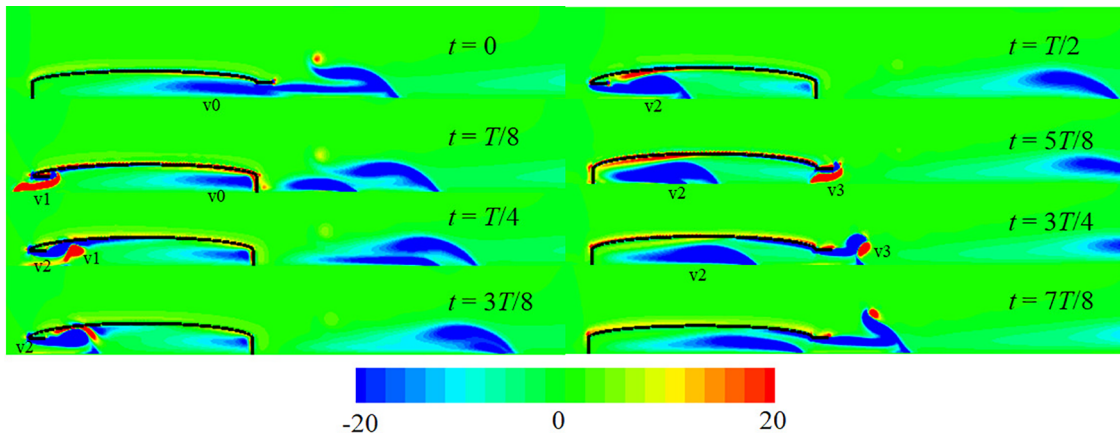


FIG. 14. Same as Fig. 13 except that $a_1 = 0.07$ and $\Gamma_m = 4.69$.

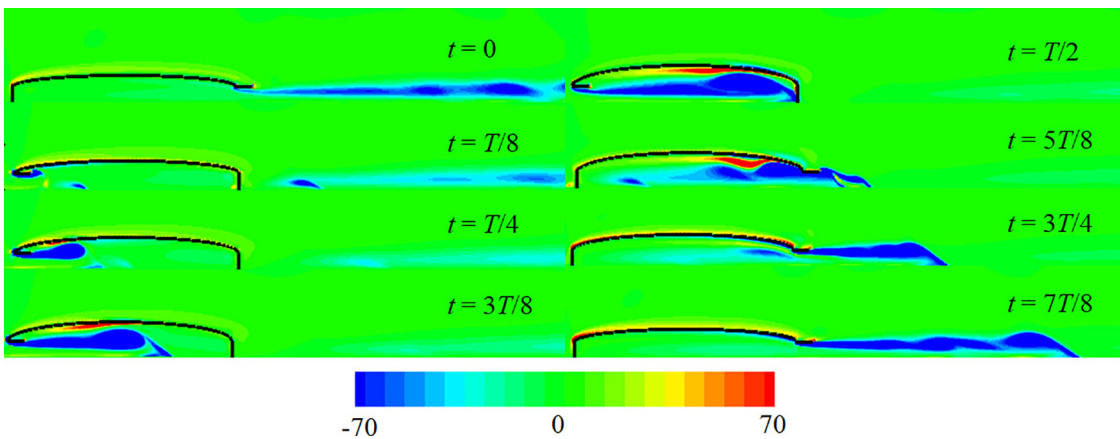


FIG. 15. Same as Fig. 13 except that $a_1 = 0.09$ and $\Gamma_m = 10.0$.

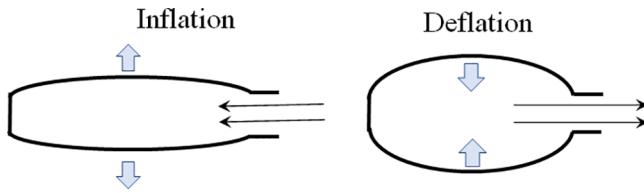


FIG. 16. A squid-like swimmer in which the refilling flow and the jetting flow are in opposite directions.

The flow fields of a case at a stroke ratio ($D=0.15$, $a_1 = 0.07$, $\Gamma_m = 4.69$) are shown in Fig. 14. In comparison with the previous case at a low stroke ratio, there are the following differences: (1) The vortices generated by the inflow and the jet (e.g., the counterclockwise vortices v_0 and v_2) are much stronger (note that in Fig. 14 the range of contour is the same as the one in Fig. 13). (2) The vortices generated by the rotations of the valves (the clockwise ones v_1 and v_3) are much weaker. This is due to the fact that in this case the inflow and outflow created by the shell expansion and shrinking are much stronger so that it takes less effort to rotate the valves (see the illustration about the inflow/outflow effect on the valves in design 0 in Fig. 8). (3) The counterclockwise vortices v_0 and v_2 generated at the inlet now travel through the chamber, exit at the outlet, and eventually join and merge with the counterclockwise vortex generated at the outlet. On the other hand, similar to the previous case, no pronounced pinchoff occurs in this case.

At a large stroke ratio of $\Gamma_m = 10$ with $D=0.15$ and $a_1 = 0.09$ (Fig. 15), the vortices created by the valves become negligibly weak. Instead, there exists secondary clockwise vorticity induced by the counterclockwise vortices in the chamber near the inner surface of the shell (see the snapshots at $t = T/2$ and $t = 5T/8$). In this case, pinch-off occurs both inside the chamber ($t = 5T/8$) and in the wake ($t = 7T/8$), where the vorticity wakes behind leading vortex rings roll into smaller vortex rings.

The discovery of both single leading vortex ring and multiple vortices following a leading one is reminiscent of the report of mode I and mode II wake patterns created by live salps.⁹ It indicates that the kinematics and range of parameters we choose in this study are physically relevant.

D. Comparison with the squid-like swimming mode

For insight, we also apply the model to simulate a squid-like swimmer in which the refilling flow and the jetting flow are in

opposite directions (Fig. 16). Toward this end, we employ the system depicted in Fig. 2 with the kinematics of deformation described in Eq. (1). The two valves are fixed so that $\theta_1 = 0$ and $\theta_2 = \pi/2$.

In Fig. 17, we plot the mean forward speed \bar{u}_b , the mean power expenditure \bar{P} , and the cost of transport CoT as functions of the stroke ratio Γ_m for our system in both the salp-like and the squid-like locomotion modes. In these simulations, we keep D fixed at 0.15 and vary a_1 between 0.06 and 0.09. It is seen that at lower values of Γ_m the squid-like mode outperforms the salp-like mode in terms of speed and CoT, whereas at higher values of Γ_m the salp-like mode performs better. For example, when $\Gamma_m = 7.27$ with the salp-like swimming, there is a 13% increase in speed and a 9% decrease in CoT. This is explained by the fact that when Γ_m is low the effects of the moving valves, i.e., the forces they generate and the energy it takes to activate them, are relatively large in comparison with those of the deformation body and the jet. These effects compromise the locomotion performance of the system. On the other hand, when Γ_m is large the influence of the moving valves becomes less important so that the benefits of uni-directional flow in the salp-like mode becomes pronounced. The advantage of this swimming mode may be further increased by optimizing the design of the valves (e.g., by using flexible valves) to minimize their hydrodynamic impact.

V. CONCLUSIONS

By using an immersed-boundary method, we studied the fluid dynamics involved in the locomotion of a salp-like swimmer. The system we consider is geometrically and kinematically simple. It includes a deformable shell and two rotational valves, one at the front and the other at the back. The coordinated deformation of the shell and rotations of the valves lead to periodic jetting and refilling so that sustained swimming is achieved. During this procedure, the internal flow is mostly uni-directional. This effectively reduces the energy loss due to dissipation inside the body.

One interesting finding of this study is the hydrodynamic interactions among the shell and the two valves. Due to these interactions, one part of the body is able to recover energy spent at another part. A particularly useful application of this phenomenon is that the two valves may be passively activated so that the mechanical design can be greatly simplified. Toward this end, the rotational directions of the valves have to be carefully chosen so that they coincide with the local flow directions at the instant when the valves are opened or closed.

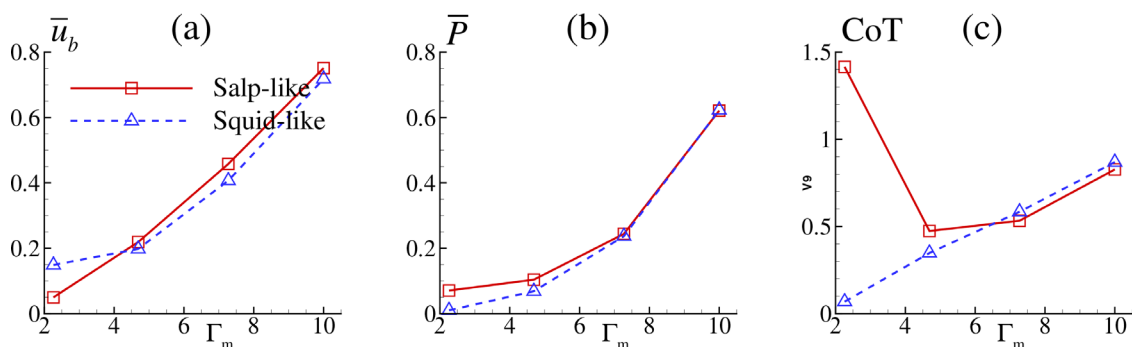


FIG. 17. Dependencies of (a) mean forward speed \bar{u}_b , (b) mean power expenditure \bar{P} , and (c) cost of transport CoT upon the stroke ratio Γ_m of salp-like or squid-like swimmers. D is fixed at 0.15 and a_1 varies between 0.06 and 0.09.

In a parametric study, we examined the effect of the stroke ratio upon the locomotion performance. The stroke ratio is varied by changing the discharged volume or the diameter of the inlet/outlet. By using CoT as a criterion, the optimal performance is reached when the stroke ratio is within the range of 4 to 7. This seems to coincide with the range in which the optimal leading vortex rings are generated. Indeed, visualizations of the flow field indicate that above this range the pinchoff phenomenon occurs behind the leading vortex rings generated by the inflow or the jet. However, we note that our problem is not a pure jetting problem since it involves not only the jetting process but also the refilling process and rotations of the valves. Thus, our finding should not be considered as definitive evidence about the role of stroke ratio on the energetic efficiency of salp-like swimmers.

In this study, the deformation of the shell and the rotations of the valves are prescribed yet the forward motion is calculated by invoking Newton's equation. An important assumption is that the structural members, i.e., the shell and the two valves, are able to store energy transferred to them from the surrounding flow and later release it. In reality, this relies on the exact mechanical design of the system. For comprehensive understanding of the problem, a coupled fluid–structure interaction study that includes the structural responses will be necessary.

AUTHOR DECLARATIONS

Conflict of Interest

The authors have no conflicts to disclose.

DATA AVAILABILITY

The data that support the findings of this study are available from the corresponding author upon reasonable request.

REFERENCES

- ¹Q. Bone and E. Trueman, “Jet propulsion in salps (*Tunicata: Thaliacea*),” *J. Zool.* **201**, 481–506 (1983).
- ²L. Madin, “Aspects of jet propulsion in salps,” *Can. J. Zool.* **68**, 765–777 (1990).
- ³J. Gosline and M. DeMont, “Jet-propelled swimming in squid,” *Sci. Am.* **252**, 96–103 (1985).
- ⁴X. Bi and Q. Zhu, “Role of internal flow in squid-inspired jet propulsion,” *Phys. Fluids* **34**, 031906 (2022).
- ⁵F. Giorgio-Serchi, A. Lidtke, and C. Laschi, “Biomimetic vortex propulsion: Toward the new paradigm of soft unmanned underwater vehicles,” *IEEE/ASME Trans. Mechatron.* **18**, 484–493 (2013).
- ⁶G. Weymouth, V. Subramaniam, and M. Triantafyllou, “Ultra-fast escape maneuver of an octopus-inspired robot,” *Bioinspiration Biomimetics* **10**, 016016 (2015).
- ⁷C. Christianson, Y. Cui, M. Ishida, X. Bi, Q. Zhu, G. Pawlak, and M. Tolley, “Cephalopod-inspired robot capable of cyclic jet propulsion through shape change,” *Bioinspiration Biomimetics* **16**, 016014 (2020).
- ⁸T. Bujard, F. Giorgio-Serchi, and G. Weymouth, “A resonant squid-inspired robot unlocks biological propulsive efficiency,” *Sci. Rob.* **6**, eabd2971 (2021).
- ⁹K. Sutherland and L. Madin, “Comparative jet wake structure and swimming performance of salps,” *J. Exp. Biol.* **213**, 2967–2975 (2010).
- ¹⁰I. Bartol, P. Krueger, W. Stewart, and J. Thompson, “Hydrodynamics of pulsed jetting in juvenile and adult brief squid *Lolliguncula brevis*: Evidence of multiple jet ‘modes’ and their implications for propulsive efficiency,” *J. Exp. Biol.* **212**, 1889–1903 (2009).
- ¹¹M. Gharib, R. Rambod, and K. Shariff, “A universal time scale for vortex ring formation,” *J. Fluid Mech.* **360**, 121–140 (1998).
- ¹²E. Anderson and M. Demont, “The mechanics of locomotion in the squid *Loligo pealei*: Locomotory function and unsteady hydrodynamics of the jet and intramantle pressure,” *J. Exp. Biol.* **203**, 2851–2863 (2000).
- ¹³X. Bi and Q. Zhu, “Efficiency of pulsed-jet propulsion via thrust-drag decomposition,” *Phys. Fluids* **33**, 071902 (2021).
- ¹⁴K. Sutherland and D. Weihs, “Hydrodynamic advantages of swimming by salp chains,” *J. R. Soc. Interface* **14**, 20180298 (2017).
- ¹⁵H. Jiang, J. Costello, and S. Colin, “Fluid dynamics and efficiency of colonial swimming via multijet propulsion at intermediate Reynolds numbers,” *Phys. Rev. Fluids* **6**, 013103 (2021).
- ¹⁶X. Bi and Q. Zhu, “Free swimming of a squid-inspired axisymmetric system through jet propulsion,” *Bioinspiration Biomimetics* **16**, 066023 (2021).
- ¹⁷R. Beam and R. Warming, “An implicit factored scheme for the compressible Navier–Stokes equations,” *AIAA J.* **16**, 393–402 (1978).
- ¹⁸K. Kim, S. Baek, and H. Sung, “An implicit velocity decoupling procedure for the incompressible Navier–Stokes equations,” *Int. J. Numer. Methods Fluids* **38**, 125–138 (2002).
- ¹⁹X. Bi and Q. Zhu, “Pulsed-jet propulsion via shape deformation of an axisymmetric swimmer,” *Phys. Fluids* **32**, 081902 (2020).
- ²⁰P. Linden and J. Turner, “The formation of ‘optimal’ vortex rings, and the efficiency of propulsion devices,” *J. Fluid Mech.* **427**, 61–72 (2001).
- ²¹P. Linden and J. Turner, “Optimal vortex rings and aquatic propulsion mechanisms,” *Proc. R. Soc. B* **271**, 647–653 (2004).